AFRL-RV-PS-
TR-2014-0101
AFRL-RV-PS-
TR-2014-0101

FDTD MODELING AND COUNTERACTION TO SCINTILLATION EFFECTS IN THE IONOSPHERE

Christos Christodoulou

Department of Electrical and Computer Engineering
University of New Mexico
Albuquerque, NM 87131

05 April 2014

Final Report

AIR FORCE RESEARCH LABORATORY
Space Vehicles Directorate
3550 Aberdeen Ave SE
AIR FORCE MATERIEL COMMAND
KIRTLAND AIR FORCE BASE, NM 87117-5776

DTIC COPY

NOTICE AND SIGNATURE PAGE

Using Government drawings, specifications, or other data included in this document for any purpose other than Government procurement does not in any way obligate the U.S. Government. The fact that the Government formulated or supplied the drawings, specifications, or other data does not license the holder or any other person or corporation; or convey any rights or permission to manufacture, use, or sell any patented invention that may relate to them.

This report was cleared for public release by the 377 ABW Public Affairs Office and is available to the general public, including foreign nationals. Copies may be obtained from the Defense Technical Information Center (DTIC) (http://www.dtic.mil).

AFRL-RV-PS-TR-2014-0101 HAS BEEN REVIEWED AND IS APPROVED FOR PUBLICATION IN ACCORDANCE WITH ASSIGNED DISTRIBUTION STATEMENT.

//SIGNED//	//SIGNED//
Maj Stephen J. Horsman	Edward J. Masterson, Colonel, USAF
Project Manager, AFRL/RVBXI	Chief, Battlespace Environment Division

This report is published in the interest of scientific and technical information exchange, and its publication does not constitute the Government's approval or disapproval of its ideas or findings.

REPORT DOCUMENTATION PAGE

Form Approved
OMB No. 0704-0188

1. REPORT DATE *(DD-MM-YYYY)*	**2. REPORT TYPE**	**3. DATES COVERED** *(From - To)*
05-04-2014	Final Report	24 Feb 2012 – 23 Feb 2014

4. TITLE AND SUBTITLE

FDTD Modeling and Counteraction to Scintillation Effects in the Ionosphere

5a. CONTRACT NUMBER
FA9453-12-1-0200

5b. GRANT NUMBER

5c. PROGRAM ELEMENT NUMBER
61102F

6. AUTHOR(S)
Christos Christodoulou

5d. PROJECT NUMBER
3001

5e. TASK NUMBER
PPM00013505

5f. WORK UNIT NUMBER
EF007987

7. PERFORMING ORGANIZATION NAME(S) AND ADDRESS(ES)
Department of Electrical and Computer Engineering
University of New Mexico
Albuquerque, NM 87131

8. PERFORMING ORGANIZATION REPORT NUMBER

9. SPONSORING / MONITORING AGENCY NAME(S) AND ADDRESS(ES)
Air Force Research Laboratory
Space Vehicles Directorate
3550 Aberdeen Avenue SE
Kirtland AFB, NM 87117-5776

10. SPONSOR/MONITOR'S ACRONYM(S)
AFRL/RVBXI

11. SPONSOR/MONITOR'S REPORT NUMBER(S)
AFRL-RV-PS-TR-2014-0101

12. DISTRIBUTION / AVAILABILITY STATEMENT
Approved for public release; distribution is unlimited. (377ABW-2014-0332 dtd 08 May 2014)

13. SUPPLEMENTARY NOTES

14. ABSTRACT

This study investigated the Finite Difference Time Domain (FDTD) modeling of ionospheric scintillation effects, which are random perturbations of electromagnetic waves propagating through the ionosphere. Ionospheric scintillation adversely affects satellite communication and global positioning system (GPS) signals. FDTD is a full-wave time-domain technique that can rigorously model electromagnetic propagation in the ionosphere, thus allowing for a better understanding of and design of numerical experiments to combat scintillation.

Methods of near-to-near field and near-to-far field transformation were implemented to enable FDTD simulation of scintillation perturbed signals at large distances. These methods were augmented by hash table based sparse data storage and parallelized evaluation to make them usable for an AFRL provided test case scenario of plane wave propagation. Research undertaken evaluated phase detection in FDTD and its compatibility with near-to-near field and near-to-far field transformation techniques needed for extrapolation based range extension. The results obtained indicate it is possible to use these techniques together with a different source implementation. A discussion of future research directions and potential improvements to the current study is also provided.

15. SUBJECT TERMS
Ionospheric scintillation, phase screen, Finite Difference Time Domain, FDTD, near-to-near field, near-to-far field, phase detection.

16. SECURITY CLASSIFICATION OF:			**17. LIMITATION OF ABSTRACT**	**18. NUMBER OF PAGES**	**19a. NAME OF RESPONSIBLE PERSON**
a. REPORT	**b. ABSTRACT**	**c. THIS PAGE**			Stephen Horsman
Unclassified	Unclassified	Unclassified	Unlimited	36	**19b. TELEPHONE NUMBER** *(include area code)*

Standard Form 298 (Rev. 8-98)
Prescribed by ANSI Std. 239.18

This page is intentionally left blank.

TABLE OF CONTENTS

LIST OF FIGURES

[1] Simpson, J., Private communication

1 Introduction

Scintillation is a disturbance in the amplitude and phase of a radio wave caused by random electron densities in the ionosphere [1]. The electron densities along the path of a propagating radio signal cause the scintillation [2]. These electron densities are a result of disturbances in the ionosphere and because the densities are the driving force behind scintillation, the ensuing change in the signal's phase is random as well [3]. Scintillation, especially around the equator, interferes with Air Force satellite communication systems as well as the Global Positioning System (GPS). Disturbances in the ionosphere are dependent on the season, solar cycle, and other variable factors [4]. Depending on the severity of the ionospheric disturbance, scintillation will be more or less pronounced.

The ionospheric scintillation problem can be considered as a signal propagation problem with the perturbations in ionosphere depicted as one or multiple random phase screens. These phase screens cause small localized perturbations in the signal phase, which will cause amplitude perturbations due to diffraction and localized interference. A popular computational technique for modeling ionospheric scintillation is the phase screen method. It calculates monochromatic plane wave propagation through any given phase screen pattern and predicts amplitude and phase perturbations. Signals that are not plane waves are analyzed by Fourier transforming the signal and performing calculations at component frequencies. Although computationally efficient, the phase screen method is limited to simulating one frequency at a time and is confined to relatively small angles [5]. In other words, this method is used to model a plane wave that does not deviate substantially from its original direction of propagation.

Recent advancements in computational capabilities provide new means of modeling the wave propagating through the ionosphere and permit analysis of scintillation characteristics in a more detailed manner. One such method is the Finite Difference Time Domain (FDTD) method, pioneered by Kane Yee in 1966 [6]. FDTD is a grid based, full-wave technique used to solve Maxwell's differential equations in the time domain. Kane Yee developed a set of finite difference equations that are central-difference in both time and space and simultaneously encompass Maxwell's equations on a microscopic and macroscopic level [7]. Yee's algorithm provides a smooth transition to a discretized form of the relationship between the electric ($\boldsymbol{E}$) and magnetic ($\boldsymbol{H}$) fields by utilizing the coupled nature of $\boldsymbol{E}$ and $\boldsymbol{H}$ given in Maxwell's equations. The robustness of this technique stems from using the information from both the $\boldsymbol{E}$ and $\boldsymbol{H}$ fields.

By using both fields, different modes, material properties, and features unique to each field are modeled through straightforward variations in the FDTD algorithm [7].

The goal of this research activity was to develop 2-D FDTD simulations for a better representation of the ionospheric scintillation effects in communications. FDTD is versatile enough to enable numerical experiments on various parts of the model (ionosphere, transmission sources, communication signal specifics, etc.) and can help in formulation of solutions that minimize scintillation effects.

Section 2 of this report provides an overview of the numerical methods. Section 3 discusses issues specific to FDTD implementation of the ionospheric scintillation problem. Section 4 presents results obtained and lessons learned. Section 5 provides recommendations for future research directions. Section 6 concludes the report.

2 Modeling and Methods

2.1 Phase Screen Method

The phase screen method models the ionosphere as a change in the incident wave's phase along each point of the wave front [1]. The number of points depend on the resolution of the chosen model. For example, the sample 1-D phase screen output[2] provided by the Air Force Research Laboratory (AFRL) for this research is a 20 kilometer wide distribution composed of 20,000 points. Therefore, the screen contains one point per meter, which results in a sampling resolution of 1 meter. The electron densities in the ionosphere form striated patterns because of their tendency to line up with earth's magnetic field [3]. This alignment is important because it leads to a dimensional simplification in the ionospheric modeling. Near the equator a 1-D phase screen is accurate because of the earth's horizontal magnetic field and because the ionosphere has a relatively insignificant thickness [1].

The phase screen method [8-10] is based on the parabolic wave equation. This is an approximation of the wave equation where the solution is weakly perturbed to deviate from a straight propagation direction. Starting from the 2-D Helmholtz equation

$$\frac{\partial^2\psi}{\partial x^2}+\frac{\partial^2\psi}{\partial z^2}+k^2n^2\psi=0 \tag{1}$$

and assuming slowly changing refractive index n, a harmonic time dependence $e^{-i\omega t}$, no changes in the y direction, and a perturbed solution

$$u(x,z)=e^{-ikx}\psi(x,z) \tag{2}$$

one can insert the prescribed solution into the equation to get

$$\frac{\partial^2 u}{\partial x^2}+\frac{\partial^2 u}{\partial z^2}+2ik\frac{\partial u}{\partial x}+k^2(n^2-1)u=0 \tag{3}$$

This equation can be factorized as

$$\left\{\frac{\partial}{\partial x}+ik(1-Q)\right\}\left\{\frac{\partial}{\partial x}+ik(1+Q)\right\}u=0 \tag{4}$$

[2] Pedersen, T., private communication

with $Q = \sqrt{\frac{1}{k^2}\frac{\partial^2}{\partial z^2} + n^2}$ an operator. Equating the first term to zero, one gets

$$\left\{\frac{\partial}{\partial x} + ik(1 - Q)\right\}u = 0 \quad (5)$$

Assuming a refractive index close to air ($n \approx 1$) and a plane-wave like solution propagating at small angles near the *x* direction, one can approximate *Q* and the square root in its definition to end up with a *parabolic differential equation* which is second degree in *z* and first degree in *x*,

$$2ik\frac{\partial u}{\partial x} = -\left\{\frac{\partial^2}{\partial z^2} + k^2(n^2 - 1)\right\}u \quad (6)$$

The phase screen method identifies irregularities in the ionosphere as layers of phase screens. Propagation through a phase screen piece or a section of free space is then calculated via analytical solutions of the parabolic differential equation.

Advantages of this method include high efficiency in calculating scintillation effects. Disadvantages are due to limitations in constructing the parabolic differential equation, such as being limited in bandwidth (constant or near-constant frequency) and propagation angle, assumption of plane wave-like solutions and oversimplified representation of ionospheric disturbances.

2.2 Finite Difference Time Domain (FDTD) Method

The FDTD method is based on a rather direct approach, where partial derivatives in space and time in half of Maxwell's equations are expressed as second-order accurate finite differences on a staggered grid of electric and magnetic fields. Maxwell's curl equations (equations 1 and 2) are split into *x*, *y*, and *z* components. The result is six coupled scalar equations for six field components.

$$\frac{\partial \boldsymbol{H}}{\partial t} = -\frac{1}{\mu}\boldsymbol{\nabla} \times \boldsymbol{E} - \frac{1}{\mu}\boldsymbol{M} \quad (7)$$

$$\frac{\partial \boldsymbol{E}}{\partial t} = \frac{1}{\varepsilon}\boldsymbol{\nabla} \times \boldsymbol{H} - \boldsymbol{J} \quad (8)$$

For 2-D implementation, differentiation with respect to *z* is set equal to zero and the six coupled equations reduce to the following scalar form (from [7]):

$$\frac{\partial H_x}{\partial t} = \frac{1}{\mu}\left[-\frac{\partial E_z}{\partial y} - (M_x + \sigma^* H_x)\right] \quad (9)$$

$$\frac{\partial H_y}{\partial t} = \frac{1}{\mu}\left[\frac{\partial E_z}{\partial x} - (M_y + \sigma^* H_y)\right] \quad (10)$$

$$\frac{\partial H_z}{\partial t} = \frac{1}{\mu}\left[\frac{\partial E_x}{\partial y} - \frac{\partial E_y}{\partial x} - (M_z + \sigma^* H_z)\right] \quad (11)$$

$$\frac{\partial E_x}{\partial t} = \frac{1}{\varepsilon}\left[\frac{\partial H_z}{\partial y} - (J_x + \sigma E_x)\right] \quad (12)$$

$$\frac{\partial E_y}{\partial t} = \frac{1}{\varepsilon}\left[-\frac{\partial H_z}{\partial x} - (J_y + \sigma E_y)\right] \quad (13)$$

$$\frac{\partial E_z}{\partial t} = \frac{1}{\varepsilon}\left[\frac{\partial H_y}{\partial x} - \frac{\partial H_x}{\partial y} - (J_z + \sigma E_z)\right] \quad (14)$$

where *x*, *y* and *z* are spatial coordinate axes, *t* denotes time, ε and μ denote permittivity and permeability, σ is electric conductivity, σ^* is magnetic loss, H_x, H_y and H_z are components of magnetic field strength, E_x, E_y and E_z are electric field components, J_x, J_y and J_z are current density components, and M_x, M_y and M_z are components of magnetization. These equations are the basis of the FDTD algorithm in 2-D. The fields in 2-D are uncoupled into two orthogonal representations. Equations (9), (10) and (14) constitute the TM_z mode and equations (11), (12) and (13) the TE_z mode. A similar dimensional reduction is performed for a 1-D implementation, which will not be covered here.

If one adopts the following convention for notational convenience

$$\begin{aligned}(i,j) &= (i\Delta x, j\Delta y)\\ u(i\Delta x, j\Delta y, n\Delta t) &= u_{i,j}^n\end{aligned} \quad (15)$$

where $\Delta x, \Delta y$ are the spatial discretization units and Δt is the unit increment in time. The first partial space derivative of the entity *u* in *x* is then written as

$$\frac{\partial u(i\Delta x, j\Delta y, n\Delta t)}{\partial x} \approx \frac{u_{i+\frac{1}{2},j}^n - u_{i-\frac{1}{2},j}^n}{\Delta x} \quad (16)$$

Similarly, the time derivative is written as

$$\frac{\partial u(i\Delta x, j\Delta y, n\Delta t)}{\partial t} \approx \frac{u_{i,j}^{n+\frac{1}{2}} - u_{i,j}^{n-\frac{1}{2}}}{\Delta t} \quad (17)$$

The discretization of the electric and magnetic field components is performed in such a way that

they are staggered in space (Figure 1) as well as time (i.e. if electric field components are expressed at time points $\left(n+\frac{1}{2}\right)\Delta t$ and $\left(n-\frac{1}{2}\right)\Delta t$, magnetic field components are expressed at $n\Delta t$ and $(n+1)\Delta t$). At this point, one can choose to collect terms in equations such that fields at time points $\left(n+\frac{1}{2}\right)\Delta t$ and $(n+1)\Delta t$ are expressed in terms of fields at earlier points in time (e.g. $\left(n-\frac{1}{2}\right)\Delta t, n\Delta t, \ldots$). This results in an *explicit marching scheme*.

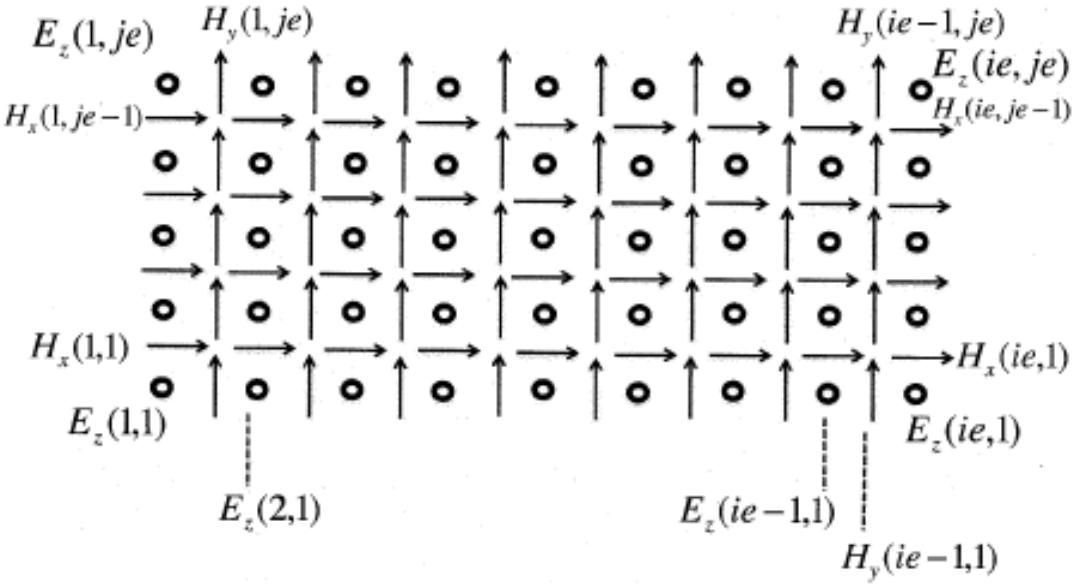

Figure 1 2-D FDTD grid with TM_z components[1]

Derivation of Yee's algorithm will not be covered here, as it can be found in many resources, for example see [7]. The result for E_z, after discretization of equation (14) is

$$E_z\Big|_{i-\frac{1}{2},j+\frac{1}{2},}^{n+\frac{1}{2}} = \left(\frac{1-\frac{\sigma_{i-\frac{1}{2},j+\frac{1}{2}}\Delta t}{2\varepsilon_{i-\frac{1}{2},j+\frac{1}{2}}}}{1+\frac{\sigma_{i-\frac{1}{2},j+\frac{1}{2}}\Delta t}{2\varepsilon_{i-\frac{1}{2},j+\frac{1}{2}}}}\right)\cdot E_z\Big|_{i-\frac{1}{2},j+\frac{1}{2}}^{n-\frac{1}{2}}$$
$$+\left(\frac{\frac{\Delta t}{\varepsilon_{i-\frac{1}{2},j+\frac{1}{2}}}}{1+\frac{\sigma_{i-\frac{1}{2},j+\frac{1}{2}}\Delta t}{2\varepsilon_{i-\frac{1}{2},j+\frac{1}{2}}}}\right)\cdot\left(\begin{array}{c}\frac{H_y\Big|_{i,j+\frac{1}{2}}^{n}-H_y\Big|_{i-1,j+\frac{1}{2}}^{n}}{\Delta x}\\ -\frac{H_x\Big|_{i-\frac{1}{2},j+1}^{n}-H_x\Big|_{i-\frac{1}{2},j}^{n}}{\Delta y}\\ -J_{source_z}\Big|_{i-\frac{1}{2},j+\frac{1}{2}}^{n}\end{array}\right) \quad (18)$$

Since the electric and magnetic field terms are staggered in time and expressed in terms of one another, the explicit marching scheme is invoked by calculating electric and magnetic field components one after another, while the time, $n\Delta t$, is increased until a predetermined value or a simulation state is reached. Spatial staggering requires calculation of field components on the entire grid at every time step, as the calculation formulas refer to field values at neighboring grid locations. This also means field values at grid boundaries cannot be calculated with the usual formulas and must be determined in other ways (i.e. by formulating *boundary conditions*).

Entities referring to material properties such as permittivity, permeability and conductivity are discretized appropriately and utilized in defining the geometry of objects on the grid. Other entities such as ad-hoc source terms *J* and *M* require special attention as they provide both means of convenience (e.g. one can inject energy into the FDTD simulation by providing a current *J* at an appropriate location) and trouble (e.g. injected currents are unphysical and such energy sources will cause spurious reflections when certain conditions are met).

One particular source type used throughout this project is known as Total Field/Scattered Field (TF/SF) source. The TF/SF technique is advantageous because it implements plane wave propagation with minimal spurious reflections. The foundation of the TF/SF technique is its dependence on the linearity of Maxwell's equations. The FDTD simulation is divided into two regions on a closed virtual boundary, named total field and scattered field regions. The total field region is enclosed by the scattered field region (Figure 2). The following relationships are asserted on the virtual boundary separating the two regions

$$\boldsymbol{E}_{total} = \boldsymbol{E}_{inc} + \boldsymbol{E}_{scat} \quad (19)$$

$$\boldsymbol{H}_{total} = \boldsymbol{H}_{inc} + \boldsymbol{H}_{scat} \quad (20)$$

where $\boldsymbol{E}_{inc}$ and $\boldsymbol{H}_{inc}$ represent the values of the incident fields and $\boldsymbol{E}_{scat}$ and $\boldsymbol{H}_{scat}$ represent the values of the scattered fields. The incident field is introduced through the virtual boundary via special field updates such that incident fields are present in the total field region but not in the scattered field region.

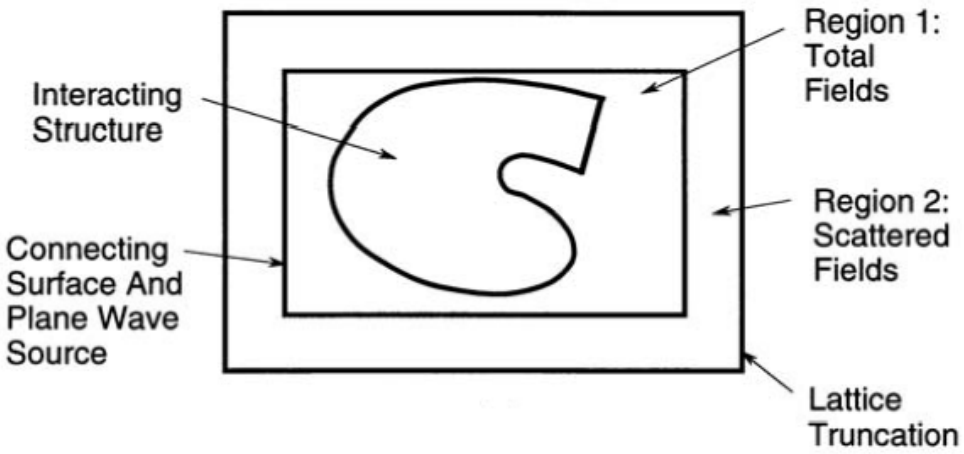

Figure 2 TF/SF space lattice depicting the total field and scattered field regions[1]

The special updates required for implementation of the TF/SF technique are achieved by fixing inconsistencies between regions. The updates are best described with a 1-D example as shown in Figure 3. In the 1-D case the virtual boundary between regions becomes a single point on each side of the total field region.

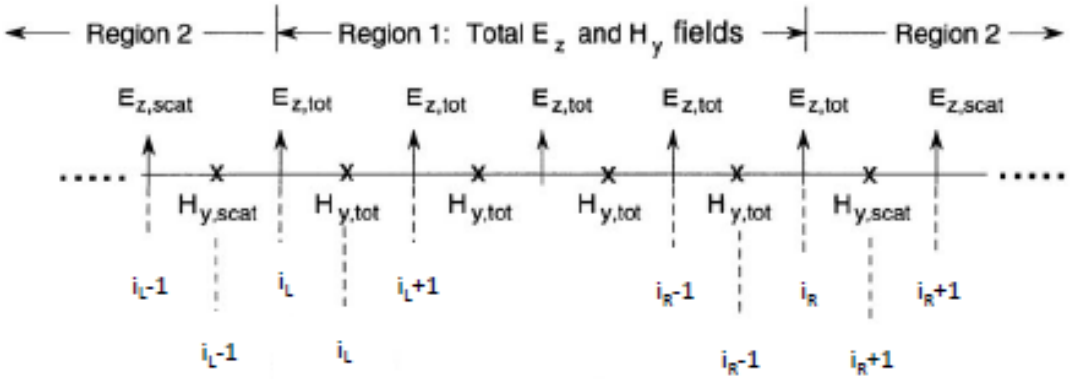

Figure 3 1-D TF/SF space lattice showing components in need of special updates[1]

At the left interface between regions 1 and 2, $E_{z,total}$ will have an inconsistent update [7]

$$E_{z,total}\Big|_{i_L}^{n+1} = E_{z,total}\Big|_{i_L}^{n} + \frac{\Delta t}{\varepsilon_0 \Delta x}\left(H_{y,total}\Big|_{i_L+\frac{1}{2}}^{n+\frac{1}{2}} - H_{y,scat}\Big|_{i_L-\frac{1}{2}}^{n+\frac{1}{2}}\right) \quad (21)$$

where i_L is the coordinate of the left TF/SF boundary. Clearly, a total field component cannot be updated by a scattered field component. To correct, the incident field term must be added to the scattered field term

$$E_{z,total}\Big|_{i_L}^{n+1} = E_{z,total}\Big|_{i_L}^{n} + \frac{\Delta t}{\varepsilon_0 \Delta x}\left(H_{y,total}\Big|_{i_L+\frac{1}{2}}^{n+\frac{1}{2}} - H_{y,scat}\Big|_{i_L-\frac{1}{2}}^{n+\frac{1}{2}} - H_{y,inc}\Big|_{i_L-\frac{1}{2}}^{n+\frac{1}{2}}\right) \quad (22)$$

where $E_{z,total}$ is now updated only by total fields. A similar inconsistency around the right boundary at i_R exists

$$E_{z,total}\Big|_{i_R}^{n+1} = E_{z,total}\Big|_{i_R}^{n} + \frac{\Delta t}{\varepsilon_0 \Delta x}\left(H_{y,scat}\Big|_{i_R+\frac{1}{2}}^{n+\frac{1}{2}} - H_{y,total}\Big|_{i_R-\frac{1}{2}}^{n+\frac{1}{2}}\right) \quad (23)$$

and it is handled in a similar way

$$E_{z,total}\Big|_{i_R}^{n+1} = E_{z,total}\Big|_{i_R}^{n} + \frac{\Delta t}{\varepsilon_0 \Delta x}\left(H_{y,scat}\Big|_{i_R+\frac{1}{2}}^{n+\frac{1}{2}} - H_{y,total}\Big|_{i_R-\frac{1}{2}}^{n+\frac{1}{2}} + H_{y,inc}\Big|_{i_R+\frac{1}{2}}^{n+\frac{1}{2}}\right) \quad (24)$$

but one must note the swapped position of the total and scattered field terms and the resulting sign reversal of the incident field term.

A numerical method is considered *numerically stable* if it does not have any numerical artifacts to cause monotonic growing or shrinking of the calculated terms. For the explicit marching FDTD formulation, simulation stability is dependent on the size of the time step. Detailed analysis, found elsewhere [7,11], leads to a relationship between the time step size (Δt) and the grid cell size ($\Delta x, \Delta y$) known as the Courant stability limit:

$$\Delta t \leq \frac{1}{c\sqrt{\frac{1}{(\Delta x)^2} + \frac{1}{(\Delta y)^2}}} \quad (25)$$

where *c* is the speed of light or electromagnetic energy propagation.

A related concept, *numerical accuracy*, refers to the finite accuracy of modeling in numerical simulations. For FDTD, it means the model must be able to adequately resolve *both* the smallest physical feature *and* the smallest wavelength in the simulation. While the Nyquist-Shannon sampling theorem [12] requires at least two mesh cells per physical feature or wavelength, common practice lore favors usage of better resolution, where 8-10 mesh cells is considered a good number. It must be noted that increasing resolution in an explicit marching based FDTD scheme will require reduction of the time step size per the Courant stability limit.

FDTD offers many advantages for ionospheric scintillation modeling, such as

- Having a full-wave simulation not limited by the parabolic differential equation or any approximations in bandwidth, propagation angle and source wave forms
- The possibility of formulating dispersive, absorptive, gain, plasma or other types of media for better representation of the ionosphere and sources of scintillation
- The ability to investigate transients and time-dependent phenomena (unavailable when a frequency-domain method is used)
- The ability to perform rigorous numerical experiments beyond insight-gathering phase
- High-performance implementation possibilities to keep simulation times at a manageable level

The disadvantages of FDTD include increased requirements for computing resources and time, intricacy of implementation, numerical dispersion and other numerical artifacts for large and/or oblong grid configurations, difficulty modeling curved shapes without approximations and difficulty using grids with many different element sizes and/or shapes.

2.3 Near-to-Near and Near-to-Far Field Transforms

Near-to-near field and near-to-far field transforms were developed to address a crucial deficiency in FDTD. Due to the way FDTD is formulated, wave propagation speed on an FDTD mesh changes slightly depending on propagation direction (a phenomenon known as numerical dispersion [7]). This means a wave front propagating in multiple directions in a large FDTD grid becomes increasingly distorted as it continues to propagate. Near-to-near field and near-to-far field transforms use different techniques to extrapolate electromagnetic field values to locations of interest without having to extend the entire FDTD grid to cover such locations.

One commonality among all such transforms is their dependence on the surface equivalence theorem, which itself is a reformulation of Huygens' principle. Surface equivalence theorem establishes the equivalence of electromagnetic fields generated by sources and scattering inside a closed surface with electromagnetic fields generated by appropriate electric and magnetic current distributions on the closed surface. The surface does not have to be a physical object and can be in any convenient shape. In the case of near-to-near field and near-to-far field transforms, surface equivalence theorem serves to replace electromagnetic fields generated inside a virtual boundary (Figure 4(a)) with equivalent surface currents on the surface (Figure 4(b)). This simplifies calculation of a number of entities such as the far field response, since the inside of the virtual boundary is devoid of electromagnetic fields and any objects inside it can be modified or removed without affecting the calculation results of interest (Figure 4(c)). If free space is present outside the virtual boundary, it becomes convenient to assume free space is

present inside the boundary. Then any calculations of interest can be assumed to take place in free space, devoid of scatterers.

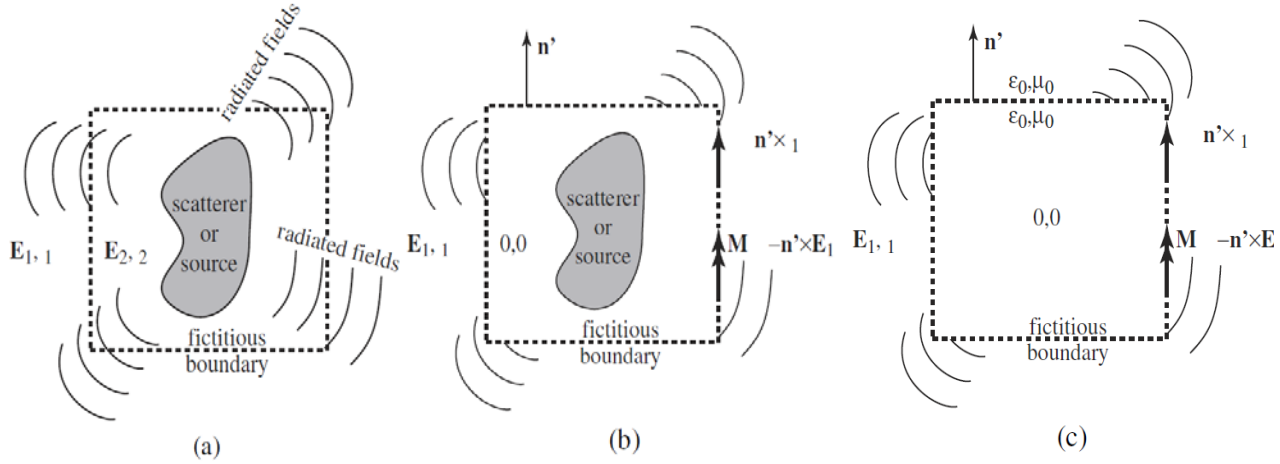

Figure 4 (a) A virtual closed boundary around a scatterer or source, shown with fields across the boundary. **(b)** Fields inside the boundary are set to zero. Fields outside the boundary are generated by surface currents on the boundary. **(c)** The scatterer or source can now be disposed of since its presence or absence is irrelevant in a region devoid of electromagnetic fields. From [13].

There are a number of near-to-near field and near-to-far field transformation methods formulated for FDTD in literature, based on integration of surface currents [7,14-22], multipole expansion [23,24], Fresnel diffraction integral [25] and Kirchhoff's surface integral [26]. Of these methods, two were employed in the course of this research: The time domain near-to-far field transform by Luebbers et al. [14] and Kirchhoff's surface integral representation (KSIR) based near-to-near field transform by Ramahi [26]. These methods will be discussed below. Further implementation details specific to the ionospheric scintillation problem can be found in Section 3.

The most fundamental equations to the time domain near-to-far field transform by Luebbers et al. [14] are given by

$$\mathbf{W}(\mathbf{r},\mathrm{t}) = \frac{1}{4\pi \mathrm{rc}}\frac{\partial}{\partial \mathrm{t}}\left[\iint_{\mathrm{S}} \mathbf{J}_{\mathrm{S}}(\mathrm{t}-\frac{\mathrm{r}-\mathbf{r}'\cdot\hat{\mathbf{r}}}{\mathrm{c}})\mathrm{dS}'\right] \quad (26)$$

$$\mathbf{U}(\mathbf{r},\mathrm{t}) = \frac{1}{4\pi \mathrm{rc}}\frac{\partial}{\partial \mathrm{t}}\left[\iint_{\mathrm{S}} \mathbf{M}_{\mathrm{S}}(\mathrm{t}-\frac{\mathrm{r}-\mathbf{r}'\cdot\hat{\mathbf{r}}}{\mathrm{c}})\mathrm{dS}'\right] \quad (27)$$

$$E_\theta(\boldsymbol{r},t) \cong -\eta_0 W_\theta(\boldsymbol{r},t) - U_\varphi(\boldsymbol{r},t) \quad (28)$$

$$E_\varphi(\boldsymbol{r},t) \cong -\eta_0 W_\varphi(\boldsymbol{r},t) - U_\varphi(\boldsymbol{r},t) \quad (29)$$

where E_θ and E_φ are the spherical far field $\boldsymbol{E}$ field components, $\mathbf{W}$ and $\mathbf{U}$ are the far-field potential vectors, $\mathbf{J}_S$ and $\mathbf{M}_S$ are the electric and magnetic currents along the virtual surface, *S*, and are expressed in retarded time, $t - \frac{\mathrm{r}-\mathbf{r}'\cdot\hat{\mathbf{r}}}{\mathrm{c}}$. This term represents the time delay between the $\boldsymbol{E}$ and $\boldsymbol{H}$ fields on *S* to their appearance at the far field point. The surface *S* should cover all sources in the FDTD simulation. If a total field/scattered field source is used, *S* will be in the scattered field (i.e. outer) region. A typical configuration for a 2-D FDTD simulation is depicted in Figure 5.

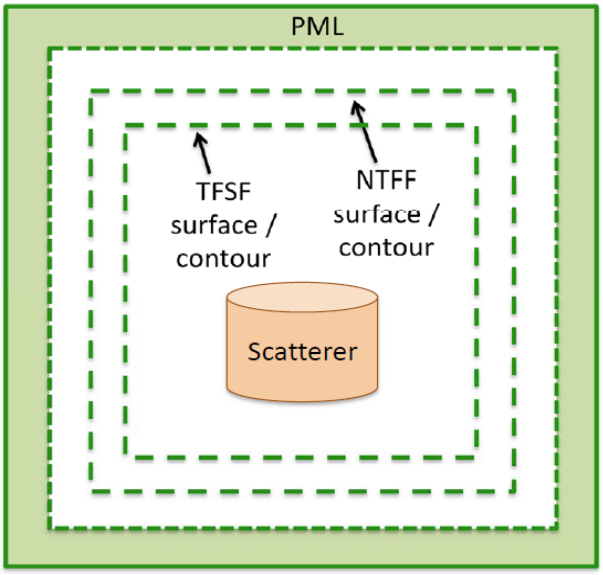

Figure 5 Typical configuration of a 2-D FDTD simulation utilizing near-to-far field (NTFF) transformation and total field/scattered field (TFSF) source. PML refers to a perfectly matched layer absorbing medium placed on the outer sides of a scattering simulation to prevent reflection of outgoing energy.

The general procedure for the near-to-far field transformation is to evaluate the integrals in equations (26) and (27). To give an example, for the surface excitation $\mathrm{M_z}$, located within a rectangular patch $\Delta x \Delta z$, the contribution from the integral in equation (27) can be written as

$$\Delta \boldsymbol{U} = \Delta U_z \hat{z} = \frac{1}{4\pi r c}\frac{\partial}{\partial t}(M_z \hat{z} \Delta x \Delta z) = \frac{\Delta x \Delta z}{4\pi r c}\frac{\partial}{\partial t}(E_x \hat{z}) \qquad (30)$$

The number of time steps until $\Delta \boldsymbol{U}$ from contributes to the far field vector potentials is given by

$$f = \frac{\mathrm{r} - \mathbf{r}' \cdot \hat{\mathbf{r}}}{\mathrm{c}\Delta \mathrm{t}} \qquad (31)$$

which is the total time delay divided by the FDTD time step. Thus, the integral in equation (27)

is written in finite difference notation as

$$U_z|_{\boldsymbol{r}}^{n+\frac{1}{2}+f} = U_z|_{\boldsymbol{r}}^{n+\frac{1}{2}+f} + \frac{\Delta x \Delta z}{4\pi r c}\frac{\partial}{\partial t}(E_x|_{r\prime}^{n+1} - E_x|_{r\prime}^{n}) \quad (32)$$

It is highly unlikely that $n+\frac{1}{2}+f$ will be an integer. This means the near-to-far field transformation will be incompatible with the general FDTD semantics. A solution is to make two fractional adjustments based on linear interpolation to the nearest integer time steps, given as

$$U_z|_{\boldsymbol{r}}^{nn} = U_z|_{\boldsymbol{r}}^{nn} + (1-a)\frac{\Delta x \Delta z}{4\pi r c}\cdot\frac{\partial}{\partial t}(E_x|_{r\prime}^{n+1} - E_x|_{r\prime}^{n}) \quad (33)$$

$$U_z|_{\boldsymbol{r}}^{nn+1} = U_z|_{\boldsymbol{r}}^{nn+1} + a\frac{\Delta x \Delta z}{4\pi r c}\cdot\frac{\partial}{\partial t}(E_x|_{r\prime}^{n+1} - E_x|_{r\prime}^{n}) \quad (34)$$

where nn is the integer truncation of the value $n+\frac{1}{2}+f$ and a is given by

$$a = \left(n+\frac{1}{2}+f\right) - nn \quad (35)$$

which represents the fractional time step between the exact delay of $\Delta\boldsymbol{U}$ and the integer time step that is just prior. Thus, $(1-a)$ is representative of the fractional time step between the exact delay of $\Delta\boldsymbol{U}$ and the integer time step that is just after it.

The transformation method outlined above is valid only if the location of interest is in the far field region of the aperture under study. This requirement is not always satisfied for the ionospheric scintillation problem, especially if one wishes to compare FDTD results against phase screen method results due to the size of the phase screen and the distance from it. As such, a more general method that can handle *both* near *and* far field extrapolation is needed. Kirchhoff's surface integral representation (KSIR) based near-to-near field transform by Ramahi [26] is one such method and was implemented during the course of this research project.

KSIR is based on Kirchhoff's surface integral, which relates a field ψ inside a closed volume *V* to the field and its derivatives on the surface of *V*,

$$\psi(x,t) = \frac{1}{4\pi}\oint_{S'} \hat{n}\cdot\left[\frac{\nabla'\psi(x',t')}{R} - \frac{\vec{R}}{R^3}\psi(x',t') - \frac{\vec{R}}{cR^2}\frac{\partial\psi(x',t')}{\partial t'}\right]_{ret} da' \quad (36)$$

where $\vec{R} = x - x'$, $R = |\vec{R}|$, $\hat{n}$ is the unit normal vector to the surface, *c* is the speed of light and

the subscript *ret* indicates the integral is evaluated at the retarded time $t' = t - R/c$. Ramahi goes on to provide part of a 3-D FDTD derivation, where $\psi = E_x$ evaluated at FDTD coordinate index $k = k_0$ of an *xy*-plane surface, $t^* = t + R/c$ is the advanced time (in lieu of the retarded time in the earlier formula), and a contribution to the integral $E_{x,k_0}(x, t_n^*)$ is given by

$$E_{x,k_0}(x, t_n^*) = F_1(n) + F_2(n+1) + F_3(n+2) \quad (37)$$

$$F_1(n) = \sum_{i'j'} \frac{-C}{2\Delta t} E_x(i', j', k_0, n) \Delta_{i'j'} \quad (38)$$

$$F_2(n+1) = \sum_{i'j'} (AD_z + B) E_x(i', j', k_0, n+1) \Delta_{i'j'} \quad (39)$$

$$F_3(n+2) = \sum_{i'j'} \frac{C}{2\Delta t} E_x(i', j', k_0, n+2) \Delta_{i'j'} \quad (40)$$

$$A = \frac{1}{4\pi}\frac{1}{R} \quad (41)$$

$$B = \frac{1}{4\pi}\frac{-\cos\theta'}{R^3} \quad (42)$$

$$C = \frac{1}{4\pi}\frac{-\cos\theta'}{cR^2} \quad (43)$$

$$\left.\frac{\partial E_x}{\partial z}\right|_{z=k_0} \cong D_z E_x(i, j, k_0, n+1) = \frac{E_x(i, j, k_0+1, n+1) - E_x(i, j, k_0-1, n+1)}{2\Delta z} \quad (44)$$

where the primed indices belong to the KSIR integration (vs. the unprimed indices referring to FDTD), $\Delta_{i'j'}$ is the area of a subsurface over which the integration is performed, *R* is the distance and θ' is the angle that the normal of subsurface $\Delta_{i'j'}$ makes with the point of interest *x*. The interpretation of equation (37) is as follows: At FDTD time step *n*, the terms $F_1(n)$, $F_2(n)$ and $F_3(n)$ are computed, and the contribution $F_1(n)$ is added to $E_x(n^*)$, where $n^* = |(n+1) + R/(c\Delta t)|_{int}$ is the propagation delay in terms of FDTD time steps, truncated to the nearest integer not exceeding its value. Similarly, at FDTD time step $n+1$, the term $F_2(n+1)$ contributes to $E_x(n^*)$, and at FDTD time step $n+2$, the term $F_3(n+2)$ contributes to the same term. Thus, at every FDTD time step, three contributions per subsurface $\Delta_{i'j'}$ are made to different E_x terms with different propagation delays.

3 FDTD Implementation of the Ionospheric Scintillation Problem

3.1 Ionosphere as a Phase Screen

One of the goals of this research project was to create a 2-D FDTD simulation of a 1-D phase screen and compare the results to a phase screen method based simulation. The phase screen simulation is representative of a plane wave traveling through the equatorial ionosphere and impinging Earth's surface. Thus the goal of the FDTD simulation was to replicate the phase, amplitude, and amplitude scintillation index (S_4) provided by the phase screen simulation at both the ionosphere and earth's surface. The amplitude scintillation index is defined in terms of root-mean-square variance of the irradiance I due to a wave [1]

$$S_4^2 = (\langle I^2 \rangle - \langle I \rangle^2)/\langle I \rangle^2 \tag{45}$$

where the brackets indicate spatial or temporal average. In order to replicate the phase screen method scenario in FDTD, a large grid with high resolution (i.e. small grid cells) and an incident plane wave are required.

The fluctuations in ionosphere were implemented in FDTD as a dielectric slab that represents the ionosphere as a simple dielectric with varying thicknesses intended to create predetermined phase delays. A plane wave source injected over a total field/scattered field source boundary propagated through the dielectric. The electric field phase was measured and compared to a reference case with a constant-thickness dielectric slab or no slab to obtain phase delay values. The phase delay values were calculated with and without a near-to-near field transformation based on Kirchhoff's surface integral representation (KSIR). In the latter, the FDTD simulation grid was elongated slightly to cover the line of extrapolation provided by the near-to-near field transformation in the former case.

The phase screen data provided by AFRL[1] for this project was a 20 *km*-wide distribution of ionosphere with a sampling resolution of 1 *m*. The phase screen contained both positive and negative phase values. Positive phase values cannot be represented by a length of dielectric slab because a wave propagating through a dielectric only experiences phase delay in comparison to free space. Therefore, every phase point is referenced to the greatest of the phase points; the greatest phase value would then have zero phase delay. The new reference is implemented

according to the following equation

$$\varphi_{ref}(x) = \varphi(x) - \varphi_{max} \quad (46)$$

where φ_{max} is the largest phase value, φ is the original array of phase screen values, and φ_{ref} is the newly referenced phase screen array. The variables are a function of *x*, which represents position along the ionosphere. By applying this equation, the maximum delay is now equal to zero and every other phase is certainly negative, i.e. delayed. This procedure is merely the equivalent of shifting the original phase screen phase values down by a constant φ_{max}. After the phases have been referenced, the slab thickness for every phase is calculated as follows:

$$l(x) = \frac{\varphi_{ref}(x)}{\left[-2\pi f\left(\sqrt{\varepsilon_r \mu_r} - 1\right)\left(\sqrt{\varepsilon_o \mu_o}\right)\right]} \quad (47)$$

where $l(x)$ is the length corresponding to a specific phase delay, $f = 250\,MHz$ is the source frequency, ε_r is the relative permittivity, $\mu_r = 1$ is the relative permeability, $\varepsilon_o$is free space permittivity, and μ_o is free space permeability. The value of $\varepsilon_r = 1.15$ was chosen to deviate from free space but also to prevent substantial reflection. Each portion of the phase screen is $l(x)$ by $1\,m$ wide. Incorporation of the slab into an FDTD simulation requires use of an FDTD mesh cell size that is fine enough to resolve variances in $l(x)$. Various simulations throughout the course of this research used resolutions of $\lambda/100$ and $\lambda/25$, where λ is the wavelength in free space corresponding to the source frequency (*f*) given above. One consequence of such a high resolution is the increased FDTD grid size. A pseudo-color rendering of the dielectric slab's first 3 *km* section is provided in Figure 6. The section of the FDTD grid that holds the slab is 252040 by 628 grid cells.

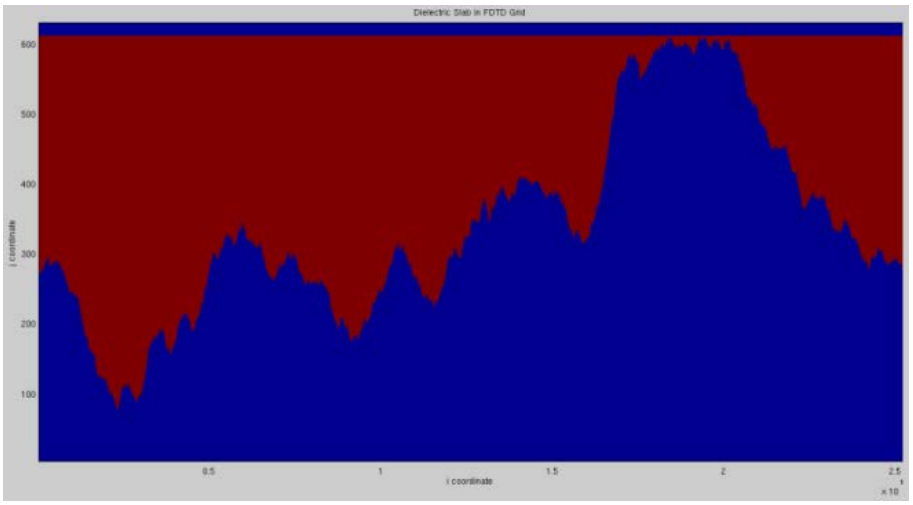

Figure 6 0-3 km region of dielectric slab in red color from FDTD. The source wave sweeps from top to bottom (i.e. flat edge of the slab is exposed first).

3.2 Implementation of Near-to-Near Field and Near-to-Far Field Transforms

The ionospheric scintillation test case provided by AFRL for this project requires a high-resolution FDTD grid ($\Delta x = \Delta y = \lambda/100 \approx 1.2\ cm$) as discussed in the preceding subsection. Such a requirement, combined with the large size of the dielectric screen model (20 *km*) and the simulated altitude from Earth's surface (300 *km*) resulted in a number of difficulties in the implementation of the near-to-near and near-to-far field transforms. The two main challenges brought in by these requirements can be summarized as:

- (i) the amount of increased processing power needed to calculate integrals over very large contour sizes in a reasonable time frame, and
- (ii) the impracticality of having to deal with very large storage arrays and array indices as the wave propagation time needed to cover 300 *km* is over 35.7 million FDTD time steps.

The first problem was addressed by taking advantage of parallel processing capabilities of modern computer workstations, clusters and computing clouds. The updates summarized in equations (33), (34) and (37) for the two transformation techniques were performed separately for each destination point of interest and as such, provide a natural way of dividing up the work. Message Passing Interface (MPI) [27] based parallelization was used in this project. MPI provides processes that can be put to work in different portions of a simulation by referring to their individual identification numbers. These processes can interact via special MPI function calls; however they do not share variables or arrays in memory. In the test case implementation, a single MPI process was used for FDTD calculations, and 63 MPI processes divided up work for

the near-to-near and near-to-far field transformation calculations. After calculation of every FDTD time step, the single MPI process broadcasted appropriate field values to the other MPI processes. After broadcasting, the single process undertook the FDTD calculations for the next time step while the other 63 processes calculated portions of the transform with the received information. At the end of the simulation the 63 processes output their portions of the final transform data into a single data file. Results obtained from the parallelized FDTD calculation do not change with the number of MPI processes used.

The second challenge was tackled by utilizing sparse data storage techniques, which are elaborated in the next section. Generally speaking, the storage technique will depend on what computer language is used for the FDTD implementation. Ecosystems of many modern programming languages have sparse storage support available in one form or another, such as sparse matrices and arrays, associative arrays and hash tables. Multiple language-agnostic storage formats such as Compressed Sparse Row, Compressed Sparse Column, and List of Lists are also available.

FORTRAN was the language of choice for the ionospheric scintillation test case implementation. This language does not natively provide an appropriate data type. The first sparse storage format tested with FDTD was Compressed Sparse Row (CSR). The updates indicated in equations (33), (34) and (37) are compatible with this 2-D sparse format if spatial coordinates (r or x) are considered as one of the dimensions and temporal coordinates (nn or t_n^*) are accepted as the other dimension. The CSR storage format divides up the 2-D data in rows and then stores nonzero elements together with their column indices. An auxiliary array indicates where rows start and end. This storage format is efficient with various linear algebra operations, but random element retrievals and element updates require a linear-time search to identify the element with the correct column index. Storing an element that was not stored previously requires expensive partial array copies. These issues tend to degrade performance for large-size systems.

After initial tests with CSR indicated low performance, portions of the FLIBS project [28] were adopted for use in FDTD. The new sparse storage support was thus based on the hash table and linked list implementations of the FLIBS project with various optimizations to improve execution speed. An iterator was also implemented on the hash table so that it could be traversed for diagnostics purposes and loop-like constructs can be executed with data from it. Hash table is

a special lookup table construct that uses a function to assign given key and value pairs an internal location. This operation can be performed faster than anything requiring a search regardless of how large the data set becomes, so long as the hash function itself can be evaluated very quickly and yields a reasonably uniform distribution of values for the data at hand. The hash function implementation of the FLIBS project was a major subject of the execution speed optimizations.

3.3 Phase Detection Method

Phase detection is the key component of ionospheric scintillation simulations in FDTD. The method used in this research operates by detecting peak amplitude timing of periodic electric field oscillations in FDTD at locations of interest. The phase delay of the incident plane wave is calculated by running the wave through the FDTD grid. The maximum values of E_z for one period of oscillation are found across the majority of the x-axis at a constant y-coordinate. In other words, E_{zmax} is calculated for every location, $(i, j_{sampling})$, where $j_{sampling}$ is located after the dielectric slab. The only i locations not sampled are locations close to the edges of the sampling region due to the possibility of edge effects creeping into the wave pattern. One period of oscillation is defined as the reciprocal of the wave frequency, 250 *MHz*, which corresponds to 4 *ns*, or approximately 143 time steps for a time step size $\Delta t = 28\,ps$ (at a spatial resolution of $\Delta x = \Delta y = \lambda/100$). Let the time step at which E_{zmax} occurs at location $\left(i, j_{sampling}\right)$ be $t_{max}(i)$. The same procedure is repeated with an identical FDTD grid without the dielectric slab. The maximum value of E_z without the slab, E_{zmaxns}, is calculated across the x-axis at the same y-coordinate, $j_{sampling}$. The time step at which the maximum occurs at every location, $(i, j_{sampling})$, to be identified as, $t_{maxns}(i)$, is recorded during this calculation. The phase delay due to the ionospheric scintillation process is calculated as

$$\varphi_{delay} = 2\pi f(t_{maxns}(i) - t_{max}(i)) \quad (48)$$

at every location $(i, j_{sampling})$.

4 Results and Discussion

FDTD simulation tests of ionospheric scintillation were performed in two stages. The first stage ensured the phase screen model worked as intended. The second stage tested the Kirchhoff's surface integral representation (KSIR) based near-to-near field transform. The simulations in the

first stage used a higher grid resolution ($\Delta x = \Delta y = \lambda/100 \cong 1.2\ cm$) while the simulations in the second stage had a lower grid resolution $\Delta x = \Delta y = \lambda/25 \cong 4.8\ cm$ to keep reasonable simulation times on the available computing resources.

A depiction of the first stage phase screen testing is provided in Figure 7. In the figure, the incident plane wave is injected through the total field/scattered field (TF/SF) contour and sweeps in a vertical direction, moving down. Thus the flat side of the phase screen is illuminated first. The phase detector captures electric field information and calculates phase delay by comparing to a simulation without the phase screen, as discussed in Section 3.3.

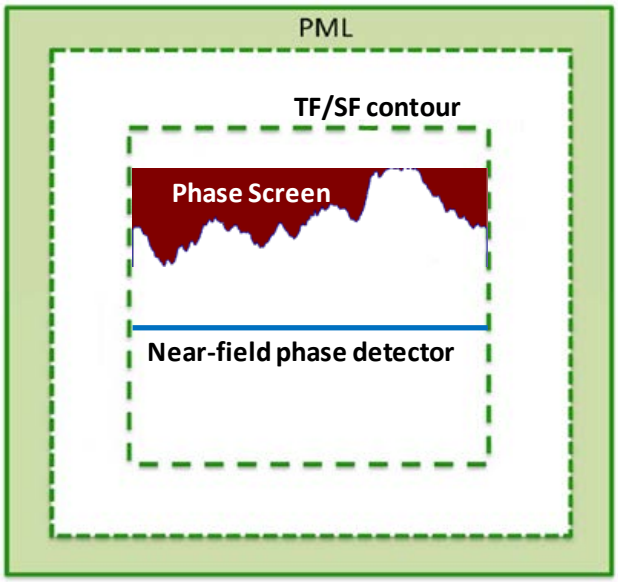

Figure 7 Typical configuration of first stage ionospheric scintillation test with plane-wave source boundary, phase screen and phase detector locations indicated. PML refers to a perfectly matched layer absorbing medium placed on the outer sides of a scattering simulation to prevent reflection of outgoing energy.

The source wave is a plane wave with a sinusoidal profile, oscillating at 250 *MHz*. The wave amplitude is attenuated at the beginning of the simulation. It is ramped up gradually to prevent any simulation instabilities due to transients that would occur otherwise. The phase information is obtained after the simulation reaches a steady state. Phase delay results are shown in Figure 8 as compared to the original data from AFRL. These results gave the researchers confidence to move forward into the second stage of testing.

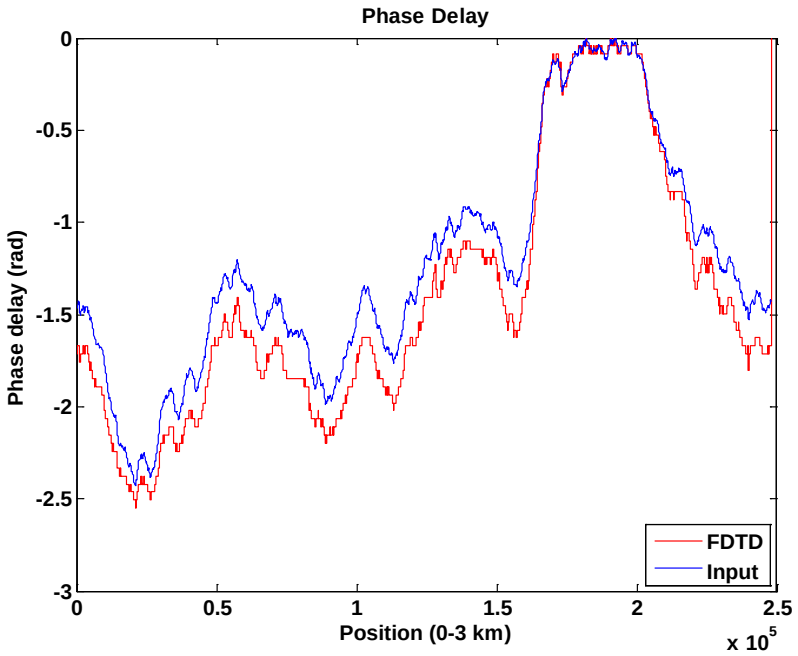

Figure 8 Near field phase delay results comparing phase delay obtained from FDTD and original phase delay data provided by AFRL for phase screen generation.

The second stage tests compared the near-to-near field transformation results (results identified as "test" or "T" in figures) with an FDTD simulation that has two sets of phase detectors (results identified as "compare" or "C" in figures), adjusted to the same locations. While these simulations are similar to the one shown in Figure 7, there are a couple key differences besides the FDTD grid resolution change. The first change is in the far-field phase detector position in the comparison case. The near-to-near field transformation contour (identified as "KSIR contour" in Figure 9(a)) is in the scattered field region (i.e. outside the TF/SF source contour). As such, the far-field phase detector in Figure 9(b) must be placed in the scattered field region as well. The second change is in the reference calculations needed for phase delay analyses. A scattered field response needed for phase detection cannot be obtained without a scatterer. As such, the reference cases corresponding to simulations in Figure 9 include a constant-height phase screen instead of only empty space. This phase screen produces a transmitted field with uniform phase response.

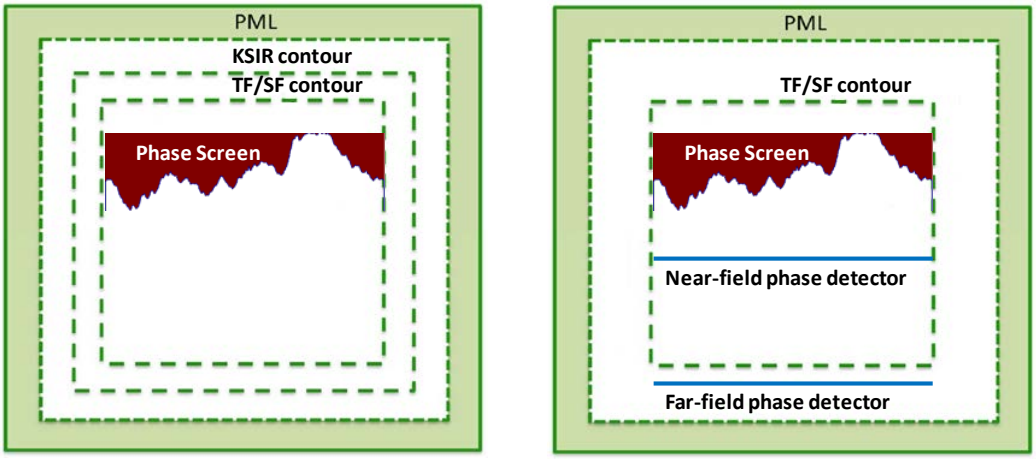

Figure 9 (a) Kirchhoff's surface integral representation (KSIR) based near-to-near field transform test configuration (results identified as "test" or "T"). **(b)** Corresponding FDTD configuration with two phase detector arrays (results identified as "compare" or "C").

Phase delay results from simulations set up as illustrated in Figure 9 are shown in Figure 10. The effect of reduced grid resolution is apparent in the near-field phase detector results (identified as "C Near"). More important, however are the fluctuations seen in the far field results. These suggest that the phase detection scheme is not working well in the scattered field region. Since it works well in the total region, the next step taken was to try to reconstruct the total field from the sampled scattered field response by adding incident field values.

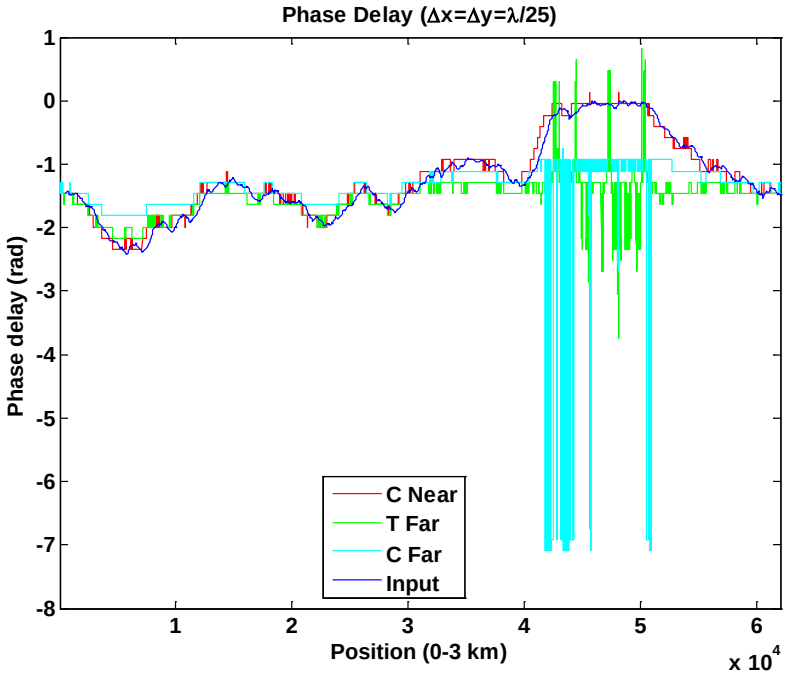

Figure 10 Phase delay results from simulations depicted in Figure 9.

Reconstruction of the total field requires the addition of appropriate incident field values to sampled scattered field values. In a 1-D sense, this reverses the change done by equation (24) of Section 2.2 on the exit side of the TF/SF source boundary. In a 2-D simulation the incident field terms are extrapolated from a 1-D auxiliary simulation for the incident field (for details refer to [7]). The same auxiliary simulation can be used for incident field reconstruction by extrapolating at the far-field phase detector location in Figure 9(b), with results shown in Figure 11. Some improvement was seen compared to scattered field-only results. Various attempts were made with heuristics rules aiming to correct phase delay jumps larger than 2π radians, smoothing and correction of the incident field signal, and reconstruction of the incident field signal as a sinusoidal wave.

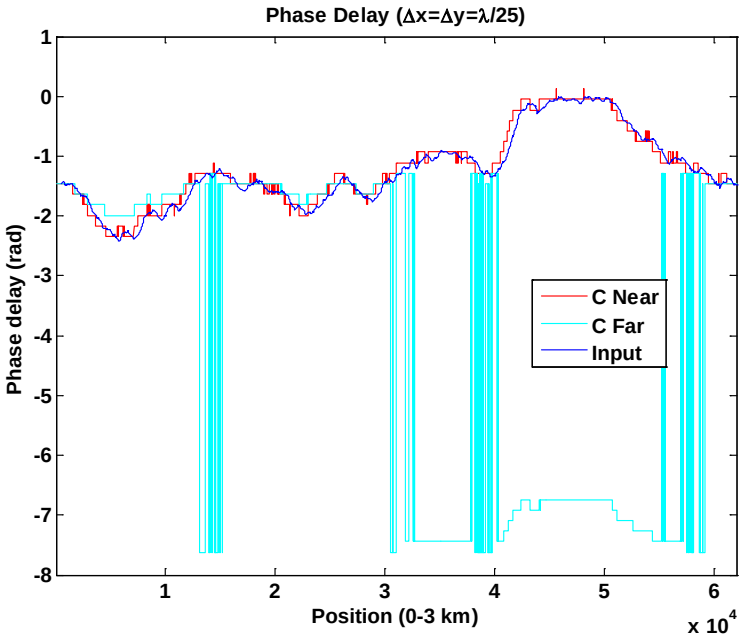

Figure 11 Phase delay results from a total field reconstruction attempt.

Next, testing efforts were concentrated on the ability of using the phase detection scheme on fields sampled in the total field region. The main problem here was how to accommodate the near-to-near field transformation into this picture. Assuming one is only interested in the phase of the fields transmitted from the phase screen and transmissions to the side are minimal under a small-angle scattering assumption, one can ignore three sides of the near-to-near field transformation contour and place it into the total field region (Figure 12). Edge effects are removed as usual in the phase delay detection process. Note that field amplitudes extrapolated from KSIR are likely not suitable for use. These assumptions can be relaxed with a different source implementation, discussed briefly in the next section and illustrated in Figure 14.

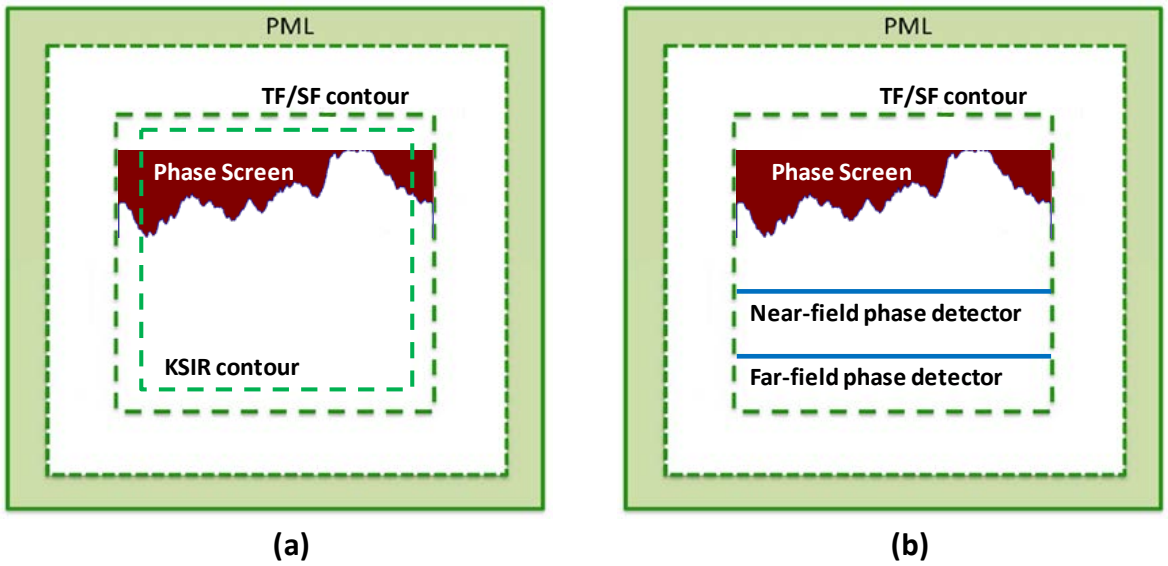

Figure 12 (a) Kirchhoff's surface integral representation (KSIR) contour placed in total field region under certain assumptions. **(b)** Corresponding FDTD configuration with two phase detector arrays.

The phase delay results are shown in Figure 13 (a). KSIR produced results that follow the phase changes mostly correctly, except for a couple jumps. These can be readjusted with simple heuristics (Figure 13 (b)), since the phase delay values cannot be positive due to the phase referencing process described in Section 3.1.

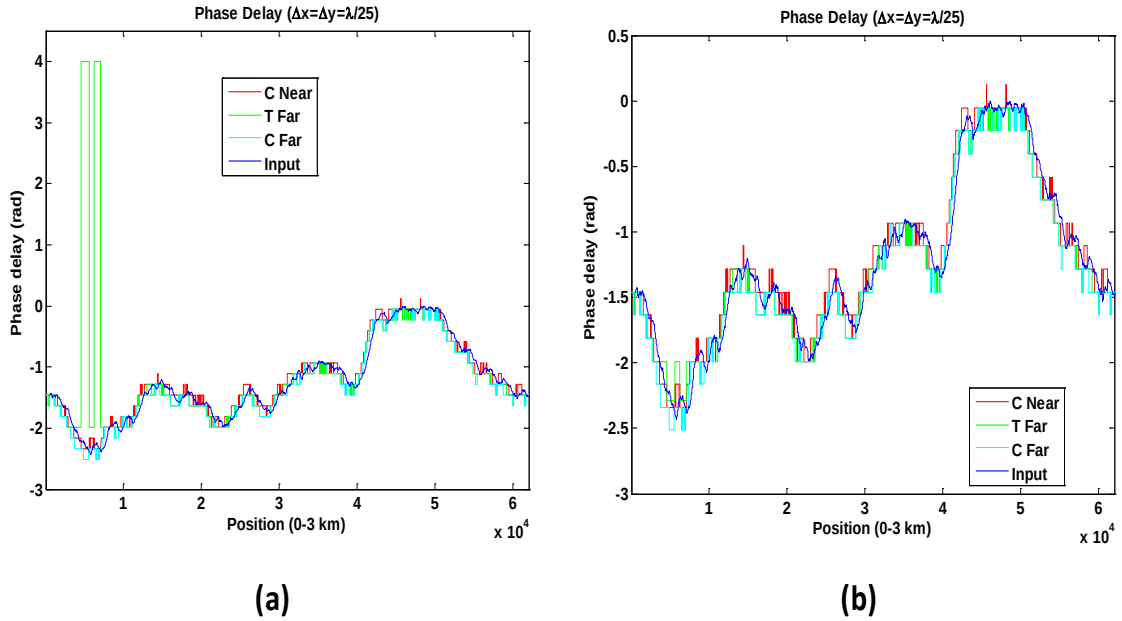

Figure 13 (a) Phase delay results from simulations depicted in Figure 12. **(b)** After translation of positive phase values by 2π radians.

5 Future Directions

This section suggests a number of technical possibilities that can improve upon the state of art attained in the course of this project. The ideas herein can be summarily divided into two categories: (i) The ones that are meant to increase numerical accuracy and efficiency of FDTD simulations for ionospheric scintillation studies, and (ii) the ones meant to improve computation performance and decrease simulation times.

The discussion in the previous section showcased the idea of using a near-to-near field transformation surface within the total field region of a total field/scattered field (TF/SF) source under certain conditions. A great improvement in accuracy can be attained by using a source that emits a narrower beam that lights up only a portion of the ionosphere model in the simulation (Figure 14). This source can be simple or very sophisticated. Choices available change from simple dipole sources [7] to more sophisticated reflectionless dipole sources [13], to eigenmode injection surfaces [29], to antenna models with various degrees of complexity [7]. Additionally, methods such as "bootstrapping", where the source wave is recorded from an auxiliary FDTD simulation for later use [7], and Huygens subgridding [30], which allows combination of a high-resolution source simulation with the main ionospheric scintillation simulation through virtual interfaces, can be utilized.

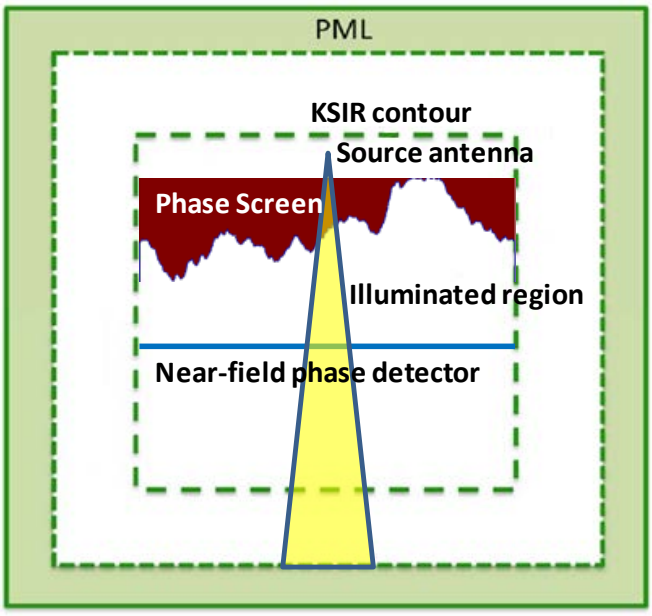

Figure 14 A source with a narrow beam profile placed into the KSIR contour. The width of the phase screen can be reduced since most of it is not illuminated by the source.

It is possible to have broadband phase determination if it is performed in the frequency domain via Discrete Fourier Transform (DFT). More details on efficient DFT implementation in FDTD can be found elsewhere [13]. DFT transformed results will be complex numbers with amplitude and phase for every frequency covered. Since DFT implies the electric field signal sampled from FDTD to be periodic or quasi-periodic in nature, this method requires some changes to the source wave (i.e. any non-periodic source wave patterns have to be repeated multiple times during the course of the simulation). Additionally, windowing and other considerations with Fourier transforms might apply.

Beach et al. [1] performed a sparse sampling study of the amplitude scintillation index (S_4). This study provides important criteria needed to get a good approximation of S_4 in the event of inadequate sampling. In this vein, practical benefit might arise if FDTD simulation results are under-sampled prior to S_4 calculations. Filtering, smoothing or other sophisticated signal correction heuristics can also be applied. Such techniques are commonly used with FDTD for certain cases, for example a Padé approximant based spectral analysis procedure can be used for acquisition of sharp resonances [7].

Performance of the simulations can be improved by using graphics accelerators. Graphics accelerators, originally developed for sophisticated scene rendering, work well on data sets with regular strides and access patterns. Many articles on FDTD acceleration reporting excellent results can be found in literature [7]. The ionospheric scintillation simulation can be accelerated similarly if the hash table/linked list design is replaced with a more cooperative one. Since the near-to-near and near-to-far field transform implementations have predictable data access patterns, it should be possible to design and implement a different data structure that is more compatible with graphics accelerators.

Last but not least, a recently developed FDTD variant [29,31,] allows calculation of stochastic mean and variance estimates with FDTD. If this method can be extended to address the problem at hand, stochastic modeling of ionospheric scintillation would provide unprecedented time savings by generating statistical information that can be obtained from hundreds or thousands of randomized FDTD models. Such statistical information is needed to assess or counter effects of scintillation on communications, such as channel fading.

6 Conclusion

This study investigated FDTD modeling of ionospheric scintillation effects. Methods of near-to-near field and near-to-far field transformation were implemented to enable FDTD simulation of scintillation perturbed signals at large distances. These methods were augmented by hash table based sparse data storage and parallelized evaluation to make them usable for an AFRL provided test case scenario.

Research undertaken evaluated phase detection in FDTD and its compatibility with near-to-near field and near-to-far field transformation techniques needed for extrapolation based range extension. The results obtained indicate it is possible to use these techniques together with a different source implementation. Finally, a discussion of future research directions and potential improvements to the current study was included. FDTD has excellent potential in terms of simulation accuracy improvements and performance improvements on modern computing hardware. This is besides its potential for stochastic modeling, possibilities for advanced antenna and ionospheric scintillation models and removal of various restrictions found in the phase screen method. It is the researchers' opinion that future research on FDTD-based ionospheric scintillation modeling will bring exciting results far beyond the reach of the current state of art.

References

[1] Beach, T. L., T. R. Pedersen, M. J. Starks, and S.-Y. Su, "Estimating the amplitude scintillation index from sparsely sampled phase screen data," *Radio Sci.*, **39**, RS5001, 2004.

[2] Rino, C. L., "A power law phase screen model for ionospheric scintillation 1. Weak scatter," *Radio Science*, **14** (6), pp. 1135-1145, 1979.

[3] Knepp, D., "Multiple Phase-Screen Calculation of the Temporal Behavior of Stochastic Waves," *Proc. Inst. Elect. Eng.*, **71** (6), pp. 722-737, 1983.

[4] Carrano, C., S., K. M. Groves, R. G. Caton, C. L. Rino, and P. R. Straus, "Multiple phase screen modeling of ionospheric scintillation along radio occultation raypaths," *Radio Sci.*, **46**, RS0D07, 2011.

[5] Wild, A. J., R.W. Hobbs, and L. Frenje, "Modeling complex media: an introduction to the phase-screen method," *Physics of the Earth and Planetary Interiors*, **120**, pp. 219-225, 2000.

[6] Yee, K. S., "Numerical solution of initial boundary value problems involving Maxwell's equations in isotropic media," *IEEE Trans. Antennas and Propagation*, **14**, pp. 302-307, 1966.

[7] Taflove, A. and S. Hagness, *Computational Electrodynamics: The Finite-Difference Time-Domain Method*, 3rd ed. Norwood, MA: Artech House, Inc., 2005.

[8] Radder, A. C., "On the parabolic equation method for water-wave propagation," *J. Fluid Mech.*, **95**, pp. 159-176, 1979.

[9] Popov, A. V. and V. V. Kopeikin, "Electromagnetic pulse propagation over nonuniform Earth surface: Numerical simulation," *Progress in Electromagnetics Research B*, **6**, pp. 37-64, 2008.

[10] C. Mätzler, *Parabolic Equations for Wave Propagation and the Advanced Atmospheric Effects Prediction System (AREPS)*, Research Report 2004-03, Bern, Switzerland: University of Bern, 2004.

[11] Courant, R., K. Friedrichs, and H. Lewy, "Über die partiellen Differenzengleichungen der mathematischen Physik", *Mathematische Annalen*, **100** (1), pp. 32-74, 1928.

[12] Shannon, C. E., "Communication in the presence of noise," *Proc. Institute of Radio Engineers*, **37** (1), pp. 10-21, 1949.

[13] Schneider, J. B., *Understanding the Finite-Difference Time-Domain Method*, http://www.eecs.wsu.edu/~schneidj/ufdtd/, 2010.

[14] Luebbers, R. J., K. S. Kunz, M. Schneider, and F. Hunsberger, "A finite-difference time-domain near zone to far zone transformation [electromagnetic scattering]," *IEEE Transactions on Antennas and Propagation*, **39** (4), pp. 429-433, 1991.

[15] Shum, S. M. and K. M. Luk, "An efficient FDTD near-to-far-field transformation for radiation pattern calculation," *Microwave and Optical Technology Letters*, **20** (2), pp. 129-131, 1999.

[16] Shlager, K. L. and G. S. Smith, "Near-field to near-field transformation for use with FDTD method and its application to pulsed antenna problems," *Electronics Letters*, **30** (16), pp. 1262-1264, 1994.

[17] Shlager, K. L. and G. S. Smith, "Comparison of two FDTD near-field to near-field transformations applied to pulsed antenna problems," *Electronics Letters*, **31** (12), pp. 936-938, 1995.

[18] Li, X., A. Taflove, and V. Backman, "Modified FDTD Near-to-Far-Field Transformation for Improved Backscattering Calculation of Strongly Forward-Scattering Objects," *IEEE Antennas and Wireless Propagation Letters*, **4**, pp. 35-38, 2005.
[19] González García, S., B. García Olmedo, and R. Gómez Martín, "A time-domain near-to-far-field transformation for FDTD in two dimensions," *Microwave and Optical Technology Letters*, **27** (6), pp. 427-432, 2000.
[20] Török, P., P. R. T. Munro, and E. E. Kriezis, "Rigorous near- to far-field transformation for vectorial diffraction calculations and its numerical implementation," *J. Opt. Soc. Am. A*, **23** (3), pp. 713-722, 2006.
[21] Coe, R. L. and E. J. Seibel, "Improved near-field calculations using vectorial diffraction integrals in the finite-difference time-domain method," *J. Opt. Soc. Am. A*, **28** (8), pp. 1776-1783, 2011.
[22] Zeng, Y. and J. V. Moloney, "Polarization-current-based, finite-difference time-domain, near-to-far-field transformation," *Optics Letters*, **34** (10), pp. 1600-1602, 2009.
[23] Oetting, C.-C. and L. Klinkenbusch, "Near-to-far-field transformation by a time-domain spherical-multipole analysis," *IEEE Transactions on Antennas and Propagation*, **53** (6), pp. 2054-2063, 2005; C.-C. Oetting, L. Klinkenbusch, "Corrections to 'near-to-far-field transformation by a time-domain spherical-multipole analysis'," *IEEE Transactions on Antennas and Propagation*, **55** (11), 3367, 2007.
[24] Klinkenbusch, L., "Time domain near-field to near-field transformation using a spherical-multipole approach," *Radio Sci.*, **46**, RS0E17, 2011.
[25] Salski, B. and W. Gwarek, "Hybrid finite-difference time-domain Fresnel modeling of microscopy imaging," *Applied Optics*, **48** (11), pp. 2133-2138, 2009.
[26] Ramahi, O. M., "Near- and far-field calculations in FDTD simulations using Kirchhoff surface integral representation," *IEEE Transactions on Antennas and Propagation*, **45** (5), pp. 753-759, 1997.
[27] The MPI Forum, *MPI: A message passing interface*, 1993.
[28] Markus, A., *FLIBS – A collection of Fortran modules*, http://flibs.sourceforge.net/, 2013.
[29] Taflove, A., A. Oskoii, and S. G. Johnson, eds. *Advances in FDTD Computational Electrodynamics: Photonics and Nanotechnology*. Boston, MA: Artech House, Inc., 2013.
[30] Berenger, J.-P., "A Huygens subgridding for the FDTD method," *IEEE Transactions on Antennas and Propagation*, **54** (12), pp. 3797-3804, 2006.
[31] Smith, S. M., C. Furse, "Stochastic FDTD for analysis of statistical variation in electromagnetic fields," *IEEE Transactions on Antennas and Propagation*, **60** (7), pp. 3343-3350, 2012.

DISTRIBUTION LIST

DTIC/OCP
8725 John J. Kingman Rd, Suite 0944
Ft Belvoir, VA 22060-6218 1 cy

AFRL/RVIL
Kirtland AFB, NM 87117-5776 2 cys

Official Record Copy
AFRL/RVBX/Maj Stephen Horsman 1 cy